# Virtual testing of impact in fiber reinforced laminates

# Virtual testing of impact in fiber reinforced laminates

10

S. Sádaba[1], F. Martínez-Hergueta[1], C.S. Lopes[1], C. Gonzalez[1,2], J. LLorca[1,2]
[1]IMDEA Materials Institute, Getafe, Madrid, Spain; [2]Polytechnic University of Madrid, Madrid, Spain

## 10.1 Introduction

Carbon fibre–reinforced polymers are nowadays extensively used in applications where outstanding mechanical properties are necessary in combination with weight saving. Good examples are the Airbus A350 XWB and the Boeing 787 Dreamliner, where fibre composites are used for up to $\approx 50\%$ of wings, fuselage sections and tail surfaces. Although the demanding in-plane loads are perfectly covered by the high strength and stiffness of the carbon laminates, it is well known that such laminates are very sensitive to out-of-plane loads coming from impacts during maintenance (i.e. tools drops) and service operations (e.g. runway debris or bird and lightning impacts) (Abrate, 1998). The traditional strategy to guarantee structural integrity is based on extensive and costly experimental campaigns in which the burden of testing is immense (up to $\approx 10^4$ tests are required for certification of an airframe structure (Cox & Yang, 2006; MIL-HDBK-17-1F, 2002)). Experimental tests include those ranging from simple coupons (tension, compression, shear) to small components (damage tolerance) up to the final composite structure (fuselage barrel or wing). Recent developments in material modelling, together with increased computational power and improvements in computing tools, are rapidly changing the aforementioned scenario of costly and time-consuming testing. Nowadays it is becoming possible to accurately predict the behaviour until failure of composite materials and small components by computer-assisted virtual testing (LLorca et al., 2011; LLorca, González, Molina Aldareguía, & Lopes, 2013).

Structural composites are manufactured by stacking different composite layers (unidirectional or woven) into a laminate with a given stacking sequence. Different damage mechanisms co-exist during composite deformation and can lead to laminate failure. Fracture due to tensile stresses parallel to the fibres is controlled by the tensile fracture of fibres, while compressive stresses along the fibres lead to kinking. Stresses perpendicular to the fibre induce failure by matrix cracking in tension or shear and interface decohesion. In addition, interply delamination is a typical failure mechanism in laminates due to the thermoelastic mismatch between adjacent plies. Accurate models to predict the failure of composite

**Structural Integrity and Durability of Advanced Composites.** http://dx.doi.org/10.1016/B978-0-08-100137-0.00010-9

laminates should include all these failure modes as well as the complex interactions among them.

Modelling of impact damage presents additional difficulties because it is important to take into account the dynamic structural behaviour and the local effects at the impact point. As a result, the use of analytical models often results in an oversimplification of the problem and thus inaccurate predictions. On the contrary, numerical simulations based on the finite element model can account for the complex constitutive behaviour of the composite material at the local (element) level together with the simulation of complex structural behaviour under complex external loads and boundary conditions.

The present chapter presents a virtual testing methodology to simulate the mechanical performance of composite laminates under impact by means of computational mesomechanics. This strategy is based on fully coupled modelization of intralaminar and interlaminar failure mechanisms in composite laminates, and is described in detail in Section 10.2. Intralaminar failure is addressed within the framework of continuum damage mechanics (CDM). Interply damage by delamination is taken into account by a cohesive crack approach that uses either cohesive elements or cohesive surfaces between adjacent plies. Two applications of this modelling strategy devoted to low- and high-velocity impact are presented in Sections 10.3 and 10.4 respectively. Future trends and expected developments in the field are briefly outlined in the last section of this chapter.

## 10.2 Mesomechanical modelling strategy of composite laminates

Individual plies are the basic building blocks in the computational mesomechanics of laminates. A virtual laminate is thus built with plies made up of different unidirectional or woven fibres (carbon, glass, aramid, etc.) embedded in a matrix (normally an epoxy resin) according to a predefined stacking sequence, as shown in Figure 10.1. The ply interfaces are also explicitly included in the model. The finite element discretization of the laminate is carried out using solid or continuum shell elements for the plies, while interface elements (or cohesive surface interactions) are used to take into account the interply delamination. This modelling strategy can account for full three-dimensional stress states, as opposed to simulations based on standard composite shell elements. Moreover, this strategy allows for analysis of the interaction between intraply and interply damage mechanisms. Obviously, computational cost limits its applicability to composite coupons or structural details and it cannot be used to model a full aeroplane.

The constitutive equation and the failure mechanisms of each ply (unidirectional or woven) are naturally constrained by the anisotropy induced by the fibre architecture

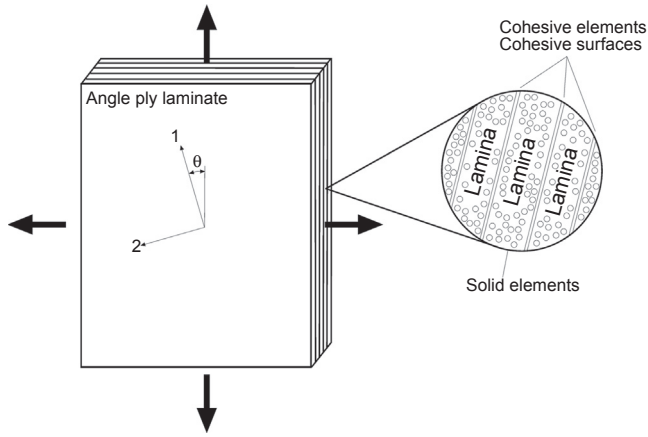


**Figure 10.1** Schematic of computational mesomechanics approach.

and the orientation of the plies. The elastic behaviour of single plies is included by means of a linear elastic orthotropic constitutive equation, while the onset of damage can be predicted using the different failure criteria available in the literature. (For instance, see Puck & Schurmann (2002); Dávila, Camanho, & Rose (2005); Pinho, Dávila, Camanho, Iannucci, & Robinson (2005); Pinho, Iannucci, & Robinson (2006a), and the relevant work of Kaddour, Hinton, & Soden (2004) in relation to the World-Wide Failure Exercise, in which different failure criteria were compared with experimental results under different loading conditions.) These failure criteria provide the critical multiaxial stress state that triggers damage in each ply for each particular failure mode (matrix splitting, fibre kinking, etc.). However, the occurrence of damage in an individual ply is not associated with the final failure of the laminate. The damage progresses in each ply, and damage interaction between plies is handled by a combination of CDM and cohesive interply decohesion, each of which is detailed below.

### 10.2.1 Intraply damage: continuum damage mechanics

CDM treats damage by assuming a homogeneous dispersion of cracks within a continuum (Kachanov, 1986; Lemaitre, 1996). Assuming a linear elastic material containing a random and homogeneous dispersion of cracks, damage is represented by damage variable $d$ expressed as

$$d = \frac{A - \overline{A}}{A} \tag{10.1}$$

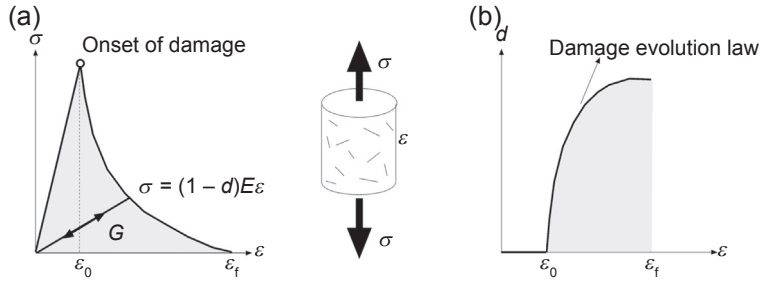


**Figure 10.2** (a) Stress−strain curve of a material under uniaxial loading according to continuum damage mechanics, where $g$ is the volumetric fracture energy (energy per unit volume) associated with the area under the $\sigma-\varepsilon$ curve. (b) Evolution of the damage variable d with strain.

where $\overline{A}$ is the net effective area (net area contributing to the load-carrying capacity of the material not including the crack area) while $A$ stands for the nominal area of the specimen (Figure 10.2). Therefore, the damage variable ranges from $0 \leq d < 1$, with $d = 0$ in the undamaged or virgin state when no cracks are present in the material and $d = 1$ in the fully damaged condition when the net effective area is $\overline{A} = 0$. If the undamaged material is a linear and elastic solid with elastic modulus $E$, the nominal stress in the damaged material $\sigma$ can be expressed as a function of the damage variable $d$ in the form

$$\sigma = (1-d)E\varepsilon = (1-d)\tilde{\sigma} \tag{10.2}$$

where $\tilde{\sigma} = E\varepsilon$ represents the effective stress in the material in the undamaged state.

The response of the material is initially elastic up to an initial strain $\varepsilon_0(d = 0)$ (damage onset); from that point, damage grows until complete fracture occurs at $\varepsilon_f(d = 1)$. The damage variable controls the evolution of damage and may depend on any internal variable (stress, strain, elastic energy, etc.). The area under the stress−strain curve corresponds with the volumetric fracture energy $g$ (energy dissipated during failure per unit of volume of material) and can be computed by integration of the stress−strain relationship along the loading path according to

$$g = \int_0^{\varepsilon_f} \sigma(\varepsilon)\, \mathrm{d}\varepsilon \tag{10.3}$$

The extrapolation of the elastic and isotropic behaviour described in Eqn (10.2) to anisotropic materials is straightforward (Matzenmiller, Lubliner, & Taylor, 1995). It will be assumed that the unidirectional fibre−reinforced composite behaves as a

linear elastic orthotropic solid, and the corresponding compliance matrix – the relation between stress and strain tensor – is expressed (in Nye notation) as

$$\begin{bmatrix} \varepsilon_1 \\ \varepsilon_2 \\ \varepsilon_3 \\ \gamma_{13} \\ \gamma_{23} \\ \gamma_{12} \end{bmatrix} = \begin{bmatrix} \frac{1}{(1-d_1)E_1} & -\frac{\nu_{12}}{E_1} & -\frac{\nu_{13}}{E_1} & 0 & 0 & 0 \\ -\frac{\nu_{12}}{E_1} & \frac{1}{(1-d_2)E_2} & -\frac{\nu_{23}}{E_2} & 0 & 0 & 0 \\ -\frac{\nu_{13}}{E_1} & -\frac{\nu_{23}}{E_2} & \frac{1}{(1-d_3)E_3} & 0 & 0 & 0 \\ 0 & 0 & 0 & \frac{1}{(1-d_4)G_{13}} & 0 & 0 \\ 0 & 0 & 0 & 0 & \frac{1}{(1-d_5)G_{23}} & 0 \\ 0 & 0 & 0 & 0 & 0 & \frac{1}{(1-d_6)G_{12}} \end{bmatrix} \begin{bmatrix} \sigma_1 \\ \sigma_2 \\ \sigma_3 \\ \tau_{13} \\ \tau_{23} \\ \tau_{12} \end{bmatrix} \tag{10.4}$$

where $E_1$, $E_2$, $E_3$, $\nu_{12}$, $\nu_{13}$, $\nu_{23}$, $G_{12}$, $G_{13}$, $G_{23}$ are the nine elastic constants that determine the elastic behaviour of the undamaged orthotropic material in the local axis material orientation, and $d_1$, $d_2$, $d_3$, $d_4$, $d_5$, $d_6$ stand for the six damage variables that control the evolution of damage during loading. Of the latter group, $d_6$ accounts for damage during in-plane shear deformation while $d_1$ and $d_2$ stand for the mechanisms associated with failure parallel and perpendicular to the fibres in unidirectional laminae (or weft and warp directions in woven structures). Additionally, the variables $d_4$, $d_5$ and $d_3$ control the respective out-of-plane shear and normal stresses $\tau_{13}$, $\tau_{23}$ and $\sigma_3$ that could potentially contribute to damage during impact loading conditions due to contact stresses with the impactors. Nevertheless, the dominant damage mechanisms are found in the laminate plane in most composite structures and therefore $d_3 = d_4 = d_5 = 0$.

The onset of damage is dictated by the failure locus of the ply given by, for instance, the LaRC04 failure criterion (Dávila, Camanho, & Rose, 2005) that has been validated

extensively for predicting the failure of uniaxially reinforced plies. The damage model used in this work is based on extending the LaRC04 plane-stress formulation proposed by Maimí, Camanho, Mayugo, and Dávila (2007a,b) to three-dimensional loading scenarios. Four failure functions, $\phi_{1+}$, $\phi_{1-}$, $\phi_{2+}$, $\phi_{2-}$, are defined in LaRC04 to account for the four in-plane damage mechanisms, and define ply failure locus as a function of the ply elastic constants and the strength for a given effective-stress state (stress obtained assuming undamaged state), as shown in Figure 10.3. The failure functions depend on the strength of the lamina in the different in-plane directions: $X_T$, longitudinal tensile strength; $X_C$, longitudinal compressive strength; $Y_T$, transverse tensile strength; $Y_C$, transverse compressive strength; and $S_L$, in-plane shear strength (Figure 10.3).

Out-of-plane shear and normal strengths in tension and compression ($S_T$, $Z_T$ and $Z_C$) should be considered when out-of-plane failure mechanisms are taken into account with additional failure functions. The onset and propagation of damage is controlled by damage-activation function $F_N$, which is associated with failure mechanisms in the longitudinal ($N = 1+, 1-$) and transverse ($N = 2+, 2-$) directions. It is expressed as

$$\text{Tensile fibre failure} \qquad F_{1+} = \phi_{1+} - r_{1+} \leq 0 \tag{10.5}$$

$$\text{Compressive fibre kinking} \qquad F_{1-} = \phi_{1-} - r_{1-} \leq 0 \tag{10.6}$$

$$\text{Tensile matrix failure} \qquad F_{2+} = \phi_{2+} - r_{2+} \leq 0 \tag{10.7}$$

$$\text{Compressive matrix failure} \qquad F_{2-} = \phi_{2-} - r_{2-} \leq 0 \tag{10.8}$$

where $r_{1+}$, $r_{1-}$, $r_{2+}$, $r_{2-}$ are the damage thresholds – internal variables of the model that are initially equal to 1 and increase monotonically during the loading history. When damage-activation functions satisfy $F_N < 0$, material response is elastic. If $F_N = 0$ and $\dot{\phi}_N \leq 0$, the state is that of elastic unloading or neutral loading. Finally, if $F_N = 0$ and $\dot{\phi}_N > 0$, there is a damage evolution controlled by the Kuhn–Tucker consistency condition

$$\dot{F}_N = \dot{\phi}_N - \dot{r}_N = 0 \tag{10.9}$$

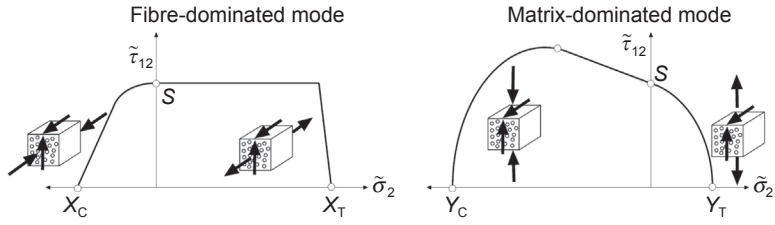


**Figure 10.3** LaRC04 failure surfaces of the virgin material represented in $\tilde{\sigma}_1 - \tilde{\tau}_{12}$ (fibre-dominated modes $\phi_{1+}$ and $\phi_{1-}$) and $\tilde{\sigma}_2 - \tilde{\tau}_{12}$ (matrix-dominated modes $\phi_{2+}$ and $\phi_{2-}$).

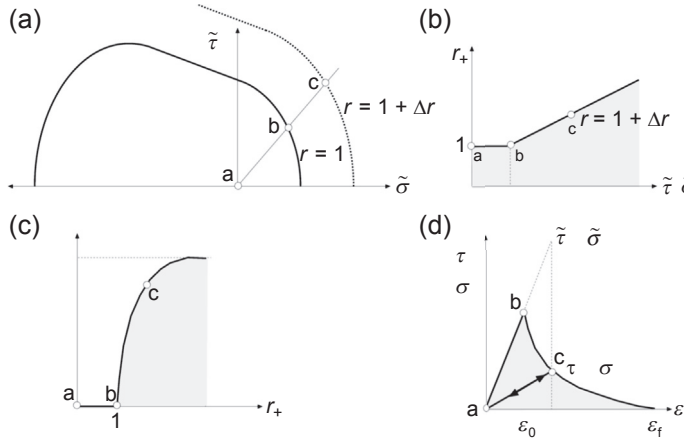


**Figure 10.4** Damage-evolution process: (a) loading in the effective-stress state, (b) increment of the internal variables of the model, (c) damage variable update and (d) softening effect in the stress−strain curve.

The procedure is shown in Figure 10.4. Initially, the load is introduced in the composite until the onset of damage occurs, represented by point b in Figure 10.4(a). At this point, the stress state is over the failure locus of the ply, and additional strain increments produce an outward movement of the damage-activation function $F_N$, leading to a corresponding increment of the damage threshold variable to fulfil the Kuhn−Tucker condition, as indicated by point c in Figure 10.4(a) and (b).

The evolution of the damage variable with respect to damage thresholds is usually taken into account through exponential expressions of the type

$$d_N = 1 - \frac{1}{r_N}\exp[A_N(1 - r_N)] \quad \text{where} \quad N = 1+,\ 1-,\ 2+,\ 2- \tag{10.10}$$

which are valid for tension and compression modes in directions parallel and perpendicular to the fibres in unidirectional composites, as shown in Figure 10.4(c). The evolution of the damage variable affecting the shear response of the composite is expressed as

$$d_6 = 1 - \left(\frac{1}{r_{2+}}\exp[A_6(1 - r_{2+})]\right)(1 - d_{1+}) \tag{10.11}$$

indicating that matrix and fibre cracks modify the shear response of the material. Crack-closure effects under load reversal cycles are also taken into account.

The coefficients $A_{1+}, A_{1-}, A_{2+}, A_{2-}, A_6$ are softening parameters that can be used to ensure mesh objectivity of the model − the model should independently dissipate the same amount of energy during failure, irrespective of the size of finite elements in the discretization. This method, known as Bazant's crack band model (Bažant & Oh, 1983), allows for regularization of the finite element problem with regard to the

size of finite element discretization. Otherwise, the model results would depend on the size of the finite element used in the mesh. The coefficients are computed from the volumetric fracture energy for a given fracture mode, $g_N$, and the corresponding material toughness of the composite material, $G_N$, measured through specific fracture tests according to

$$g_N = \frac{G_N}{l_{\text{ch}}} \tag{10.12}$$

where $l_{\text{ch}}$ is the characteristic length of the finite element used in the simulations.

The elastic properties of unidirectional plies ($E_1$, $E_2 = E_3$, $\nu_{12} = \nu_{13}$, $\nu_{23}$, $G_{12} = G_{13}$, $G_{23}$) and ply strengths ($X_T$, $X_C$, $Y_T$, $Y_C$, $S_L$) can be measured using standard tests or estimated by means of computational micromechanics (LLorca et al., 2011, 2013; Canal, González, Segurado, & LLorca, 2012; González & LLorca, 2007). The four components of fracture toughness, associated with longitudinal failure in tension and compression ($G_{1+}$ and $G_{1-}$ respectively) and transverse failure in tension and shear ($G_{2+}$ and $G_6$ respectively) can also be measured from independent tests. For instance, $G_{2+}$ can be obtained using a standard test procedure devised by the ASTM, while $G_{1+}$ and $G_{1-}$ are determined from compact tension and compact compression tests developed by Pinho, Robinson, & Iannucci (2006b). Transverse failure in shear $G_6$ can be measured using the four-point bending end-notched flexure test proposed by Martin, Elms, & Bowron (1998). Finally, the fracture toughness $G_{2-}$ can be calculated from $G_6$ and the ply fracture angle for pure transverse compression (Maimí et al., 2007a,b).

### 10.2.2 Interply delamination: cohesive crack model

Interply delamination is a typical failure mode in composite laminates because of the stress concentration induced by the elastic mismatch of adjacent plies with different fibre orientations. The crack path is defined a priori, and progressive interply delamination under mixed-mode loading can be analysed by means of a cohesive crack model coupled with interface elements between the ply surfaces (Camanho & Dávila, 2002; Turón, Camanho, Costa, & Dávila, 2006) or cohesive interactions between surfaces (Abaqus, 2014).

The mechanical behaviour of the interface can be expressed in terms of a traction–separation law relating the displacement jumps between adjacent plies of the interface with the traction vectors acting on it. For instance, Figure 10.5 shows a sketch of an

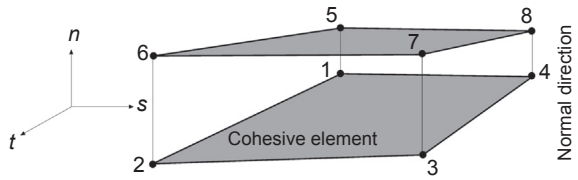


**Figure 10.5** Interface element notation.

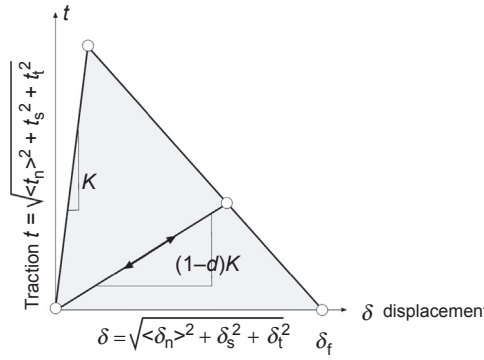


**Figure 10.6** Constitutive equation for the cohesive crack under mixed-mode loading.

eight-node standard cohesive element. In the absence of damage, the interface elements are linear elastic with an initial stiffness given by $K$, where $K$ can be treated as a numerical parameter that should be large enough to ensure the displacement continuity at the interface, avoiding distortions of the stress fields in the absence of damage (Figure 10.6). The traction vector is given by $\overrightarrow{t} = t_n \overrightarrow{e}_n + t_s \overrightarrow{e}_s + t_t \overrightarrow{e}_t$ being the traction components $t_n = K\delta_n$, $t_s = K\delta_s$ and $t_t = K\delta_t$, and $\overrightarrow{\delta} = \delta_n \overrightarrow{e}_n + \delta_s \overrightarrow{e}_s + \delta_t \overrightarrow{e}_t$ as the respective conjugate displacement jump at the interface. The onset of damage occurs when the traction vector acting on the interface reaches the interface strength dictated, for instance, by a quadratic interaction stress criterion that could read as

$$\left(\frac{\langle t_n \rangle}{N}\right)^2 + \left(\frac{t_s}{S_S}\right)^2 + \left(\frac{t_t}{S_T}\right)^2 = 1 \tag{10.13}$$

where $N$, $S_S$ and $S_T$ stand for the interface strength in tension and shear in the s and t directions, respectively, and $<>$ stands for the Macaulay brackets. As the interply is a matrix-rich region, the matrix strength in tension and shear are appropriate lower bounds for these parameters, although corresponding ply normal and shear strengths can be used in the absence of more specific data. Therefore, $N \approx Y_T$ and $S_S = S_T \approx S_L$.

After the onset of damage, the stress transmitted by the cohesive crack is reduced according to the damage parameter $D$, which evolves from 0 in the absence of damage to 1 when the physical interaction across the crack disappears. The actual reduction of the stress transferred through the cohesive crack is defined by the slope of the softening region in the $t-\delta$ constitutive equation, which depends on the interply strength and fracture toughness $G_c$ (the area under the $t-\delta$ curve), as shown in Figure 10.6.

The interply toughness depends on mode mixity and can be determined according to the Benzeggagh–Kenane criterion (Benzeggagh & Kenane, 1996) as

$$G_c = G_{Ic} + (G_{IIc} - G_{Ic})\left\{\frac{G_s + G_t}{G_n + G_s + G_t}\right\}^{\eta} \tag{10.14}$$

where $G_n$, $G_s$ and $G_t$ are the work done by the tractions and their conjugate relative displacements in the normal, first and second shear directions, respectively. Interply fracture toughness is represented by $G_{Ic}$ and $G_{IIc}$ in modes I and II respectively (it was assumed again that $G_{IIc} = G_{IIIc}$), and $\eta$ determines the increase in toughness with the amount of mode mixity. Standard mixed-mode fracture tests are used to obtain $G_{Ic}$, $G_{IIc}$ and $\eta$. Except for the parameter $\eta$, the material properties required in order to define the cohesive model are common to those required in defining the intraply damage model. In order to define the parameter $\eta$, the mixed-mode bending test proposed by Crews and Reeder (1998) should be carried out − a standard value of $\eta = 1.75$ is commonly used.

The choice of the cohesive element thickness $e_{coh}$ and stiffness $K$ is also a common source of problems during explicit integration in finite element codes. Typically, the stable time increment $\Delta t$ used in central differences explicit integration schemes is based on a conservative estimation using the Courant number. The stable time increment is element dependent, and the local estimator to be used for cohesive elements is

$$\Delta t = l_{ch}\sqrt{\frac{\overline{\rho}}{K}} \tag{10.15}$$

where $l_{ch}$ is the in-plane characteristic length of the cohesive element and $\overline{\rho}$ the surface density. Therefore, the thinner the cohesive elements, the lower the stable time increment required for the integration of the motion equations, thereby increasing computational efforts. As a rule of thumb, choosing the cohesive element thickness as a small fraction of the ply thickness (for instance, $e_{coh} \approx 0.05 e_{ply}$) and estimating the penalty stiffness as $K \approx E_{resin}/e_{coh}$ leads to reasonable results in terms of accuracy and computing time. Mass scaling of the cohesive elements can also improve the computational efficiency, while accuracy is not affected by simply adding a small artificial mass to the cohesive element. Cohesive models also present a characteristic length proportional to the length of the fracture process zone, usually given by

$$l_{ch} = \gamma \frac{E_M G_M}{X_M^2} \tag{10.16}$$

where $E_M$, $X_M$ and $G_M$ are the material modulus, strength and fracture toughness, respectively, while $\gamma$ a dimensionless parameter of the order of unity. In order to adequately capture the stress distribution within the fracture process zone, the cohesive element length should be adapted to this characteristic length. Cohesive surface modelling (Abaqus, 2014) offers capabilities similar to those of standard cohesive elements. In this case, the constitutive behaviour of the cohesive layer is lumped into a surface-to-surface interaction following the classical formulation of contact problems. This simulation strategy allows for definition of nonconformal meshes between adjacent plies, alleviating the discretization problem that arises when complex geometries and stacking sequence layups are used.

## 10.3 Use case 1: low-velocity impact due to drop weight

Finite element models were developed in Abaqus/Explicit to simulate several physical processes that occur during low-velocity impact on composite laminates. The emphasis was placed on the correct geometric representation of the impact problem, including loads, boundary conditions, material behaviour and contact conditions between the bodies. Impacts on specimens with the same ply layup, $[\pm 45/90/0/45/0_4/-45/0_2]_s$, were simulated with different impact energies, and the predictions were in good agreement with experimental results reported in Lopes, Seresta, Gürdal, Camanho, & Thuis (2009). The 4.368-mm-thick specimens included 24 AS4/8552 plies with a nominal individual thickness of 0.182 mm. Since some plies were clustered at 0°, the effective number of plies was only 15. VUMAT user subroutines were used to implement the CDM model that accounts for intraply damage, while cohesive interactions were used to address interply delamination.

### 10.3.1 Model definition

The geometry and boundary conditions described in the 'standard test method for measuring the damage resistance of a fibre-reinforced polymer matrix composite to a drop-weight impact event' of ASTM D7136 are shown in Figure 10.7. Composite panels of 150 × 100 mm$^2$ were fixed between a steel support and four rubber clamps. The support has a free area of 125 × 75 mm$^2$ in the centre, and the panel was placed on the support fixed by the four rubber clamps. In the simulations, the support was considered a rigid solid in contact with the panel. The rubber clamps were also rigid and in contact with the specimen, and each one transmitted a vertical force of 1 kN to the specimen. The impactor was modelled as a rigid body with a lumped mass equal to

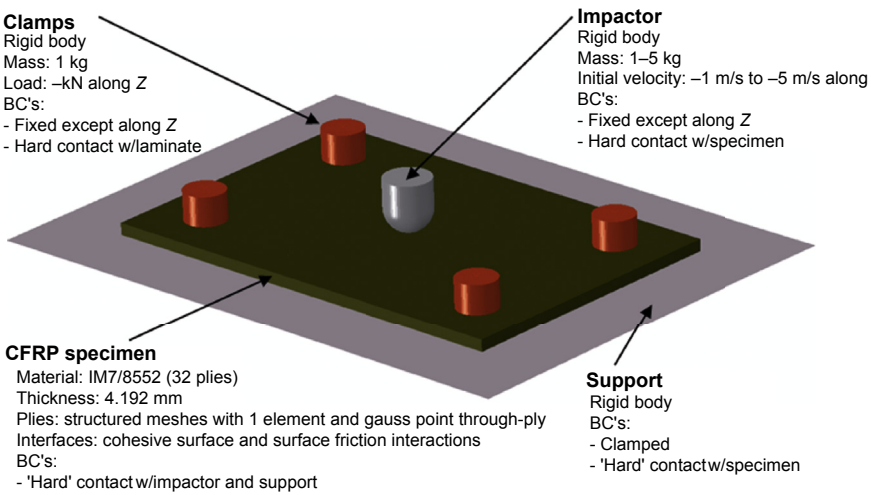


**Figure 10.7** Virtual low-velocity impact test setup.

the experimental one. It has a sphere-shaped impact surface with a diameter of 16 mm. An initial velocity in the vertical direction is prescribed to the impactor, simulating the impact velocity measured during the tests.

The finite element model has four distinct parts: specimen, impactor, bottom support and rubber clamps. The impactor was modelled as a rigid analytical surface associated with the pointwise mass. The bottom support was a rigid body discretized with rigid elements. The composite specimen was discretized in two different zones kinematically tied together. Far away from the impact point, only the elastic behaviour is taken into account, by means of a single layer of continuum shell elements that represent the whole laminate. In the region around the impact point, each ply was independently modelled with one layer of solid 'C3D8R' elements. An enhanced-strain method was used to prevent hourglassing of the elements with reduced integration. The interfaces between each ply were modelled with a penalty contact algorithm coupled with cohesive surfaces to simulate delamination by means of the traction−displacement laws described above, and to prevent interpenetration of the delaminated surfaces (Abaqus, 2014).

The simulation of cracking and fracture by means of CDM models is mesh-dependent. There are two main sources of mesh dependency, mesh alignment and element size. Cracks tend to follow mesh lines and therefore random meshing may cause the incorrect prediction of crack propagation. In the case of matrix cracking, this may influence delamination patterns as well, since there is a strong interaction between these two failure modes, especially in low-velocity impact situations. In the present work, each ply was meshed independently, with mesh lines aligned with fibre orientations to facilitate propagation of matrix cracking following the fibre direction. This creates nonconformal ply meshes through the thickness of the laminate, an issue that is easily dealt with by means of the ply-to-ply contact algorithm coupled with cohesive surfaces.

The mesh regularization to minimize effects due to element size was carried out using the element characteristic length $l_{ch}$ as a variable (Maimí et al., 2007a,b) (see Figure 10.8). In nonaligned meshes, $l_{ch}$ is the typical distance across the element surface that favours the use of square surface elements. In material-aligned meshes, two independent characteristic lengths, $l_{ch}(1+, 1-)$ and $l_{ch}(2+, 2-, 6)$, can be devised

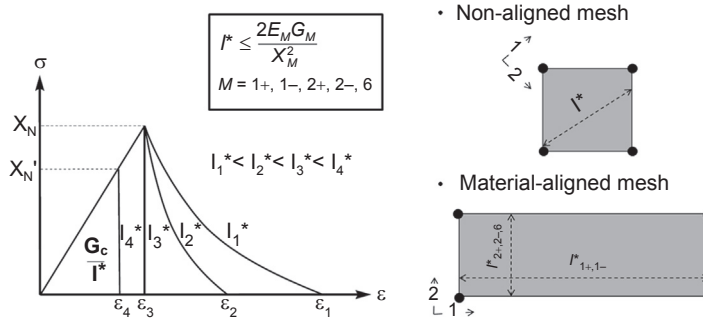


**Figure 10.8** Mesh-regularization strategy.

and used with fibre- and matrix-dominated damage modes, respectively. In this work, $l_{ch}(1+, 1-) = 0.6$ mm and $l_{ch}(2+, 2-, 6) = 0.3$ mm.

Element erosion is important in impact analysis in order to prevent high element distortions that reduce the stable time increment during explicit integration, and allow for a good description of the kinematics of the impact process, from crack opening and fibre entanglement to specimen perforation. In the current analyses, finite elements were eroded when the fibre damage variable $d_{1+}$ reached a value of 0.999, or the transverse tensile damage variable $d_{2+}$ reached a value of 0.99.

Contact between the impactor and laminate was modelled by the 'general contact algorithm' in Abaqus/Explicit, which uses a penalty enforcement contact method. This contact formulation is also applied between the different composite layers when the cohesive surfaces become fully damaged. Friction is introduced between all the contacting surfaces with a friction coefficient $\mu$. The friction coefficient between surfaces depends on the materials in contact and on surface quality. Several authors have studied the friction between metals and composite laminates, as well as between delaminated surfaces (Sung & Suh, 1979; Schön, 2000). In the last case, the friction coefficient was a function of the angle between fibres in adjacent plies, which can be as low as 0.2 for 0°/0° interplies and as high as 0.8 for 90°/90° interplies. In this work, an average friction coefficient of 0.5 was applied between ply surfaces, independent of the interply angle. A value of $\mu = 0.3$ was used for metal−laminate contact (impactor−laminate and laminate−supports).

The number of elements in the finite element meshes was over one million. On average, each run takes 48 h to complete using a cluster of 40 Intel Ivy Bridge 2.6 GHz CPUs. Such a long calculation time is a direct result of the small stable time increment required by Abaqus/Explicit to handle elements of 0.6 mm by 0.3 mm in size. Mass scaling was applied to the model while keeping the total mass increase under 2%.

### 10.3.2 Simulation results

Figure 10.9 shows the specimen at maximum impactor penetration for four impact energies. It can be clearly seen that damage increases rapidly with the impact energy of 19.7−50.8 J. The only damage found at 19.7 J was fibre splitting in the centre of the specimen at the rear surface. This phenomenon is due to the transverse tension of the 45° ply. Fibre splitting was extended towards the edges of the specimens at 29.7 and 39.4 J. At these energies, damage becomes visible at the inner plies in the form of matrix cracks and fibre breakage. The impactor partially perforated the specimen at 50.8 J, as indicated by the large penetration of the indentor into the specimen as well as the damage pattern.

The experimental and simulated force versus displacement curves are plotted in Figure 10.10 for tests carried out with 19.7, 29.7, 39.4 and 50.8 J. The oscillations in the experimental load versus displacement curves were due to dynamic coupling between the specimen and the metallic supports that was not replicated by the explicit finite element simulations, inevitably including unrealistic viscous-dissipation mechanisms that damped the dynamic response. However, the agreement between

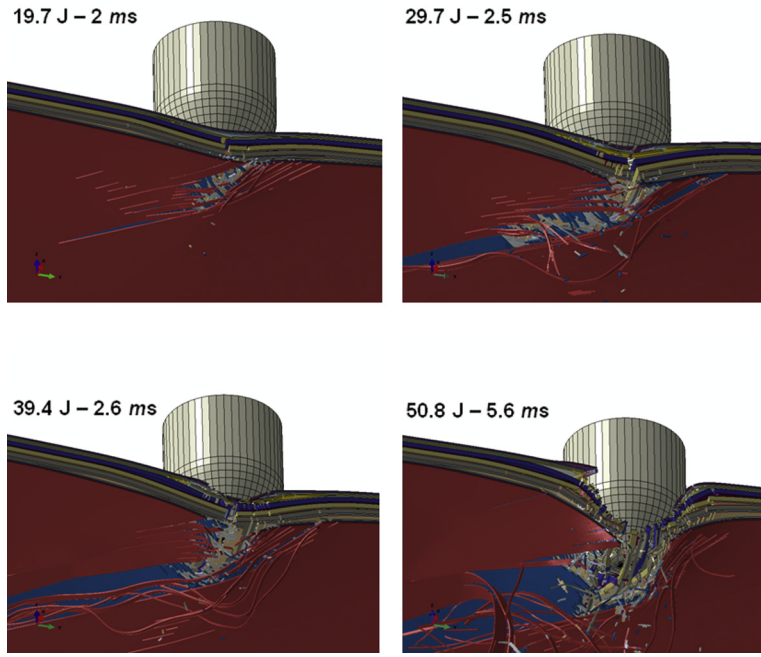


**Figure 10.9** Deformation and damage mechanisms at maximum impactor penetration for four impact energies.

experiments and simulations is very good. The maximum impact force was well predicted, with the exception of the tests with the largest impact energies, in which numerical simulations overestimated the maximum load.

Regardless of the dynamic oscillations, the initial stiffness of the specimens is generally well predicted by the numerical model. The maximum impactor displacements were also in good agreement with the experimental results except for the impact at 50.8 J. The specimen was close to perforation with this impact energy. A precise result is more difficult to obtain under these circumstances, and the predicted unloading curves differed from the experimental ones. There was a permanent indentation in the specimen after impact due to intraply frictional resistance, fibre entanglement and matrix plastic behaviour under shear deformation. However, permanent indentation was not captured by the accelerometer at the impactor tup because there was a loss of impactor−specimen contact, and the force measured by the load cell was reduced to zero before the composite specimen sprang back. The impact simulations took into account intraply frictional resistance and fibre entanglement. Furthermore, they were highly damped, and there was less loss of contact between impactor and specimen before total spring-back. Therefore, the unloading curves tend to better simulate the permanent indentation values, as shown in Figure 10.10. The experimental and numerical simulations of permanent indentation in the composite specimen impacted with 29.7 J are shown in Figure 10.11.

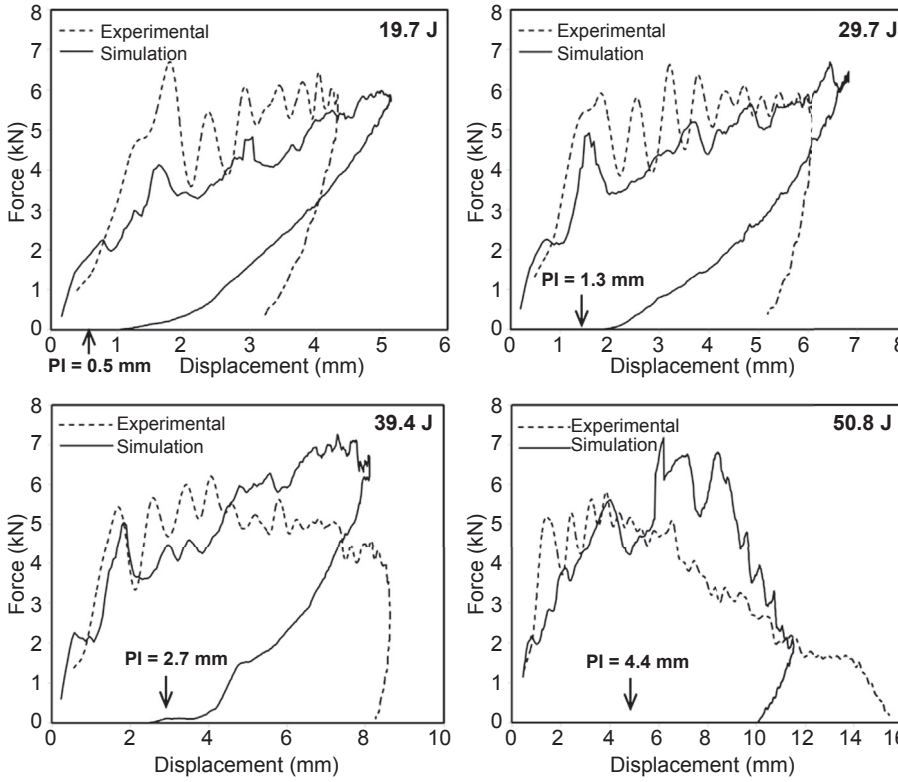


**Figure 10.10** Load versus displacement curves of low-velocity impact tests at different impact energies (PI = permanent indentation − experimental).

The predicted damage footprint is roughly the superimposition of delaminations at all interfaces, since the other damage modes are concentrated in narrow regions around the impact point. The predictions for the damage footprint are compared in Figure 10.12 with the actual damage footprint measured by C-scan (Lopes et al., 2009). Considering the limitations of the ultrasonic C-scan technique, the simulated projected damage area in each configuration agreed reasonably well with the experimental results for all impact energies, especially for the 19.7 J case. The models were relatively accurate in the identification of delamination of the rear ply (45°) triggered by face-ply matrix cracking and fibre splitting.

Both the experimental and numerical results show that the damage footprint did not increase much for impact energies above 30 J. This was because fibre breakage replaced delamination as the main damage mode, and the impactor began to penetrate the specimen, as shown in Figure 10.9, without further delamination.

Matrix cracking and fibre breakage appeared to be the first damage phenomena to occur in composite laminates undergoing impact loads, especially around the impact point. Above an impact energy threshold, which for the present configuration was

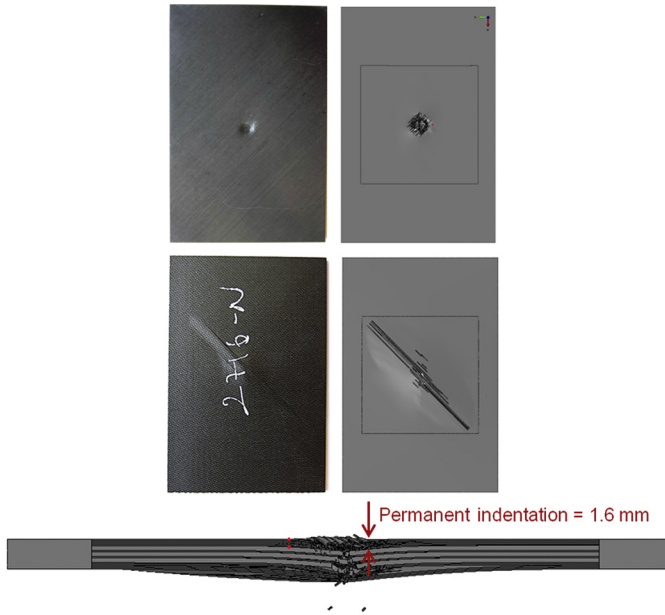


**Figure 10.11** Experimental and simulated permanent indentation on the 29.7 J impact specimen due to intraply friction and fibre entanglement.

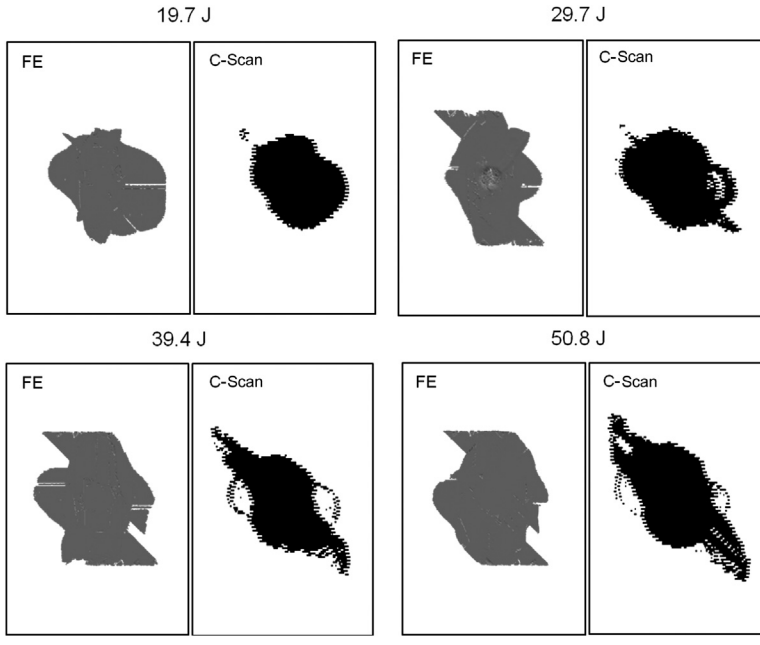


**Figure 10.12** Simulated impact damage contours compared with C-scan results.

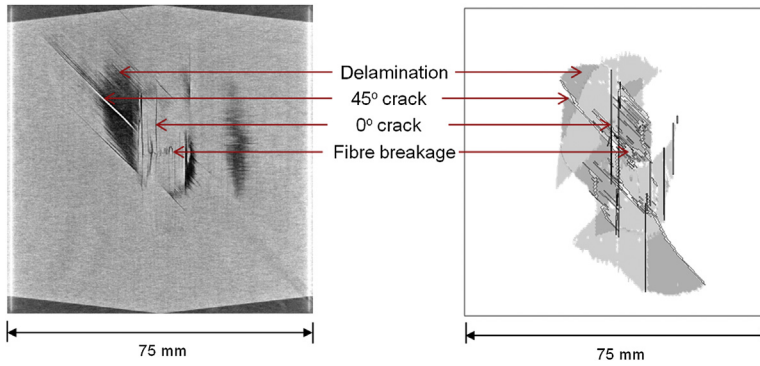


**Figure 10.13** X-ray tomography section of the composite specimen impacted at 19.7 J compared with simulation results. The X-ray tomography section shows a planar section of the impacted specimen at 3.6 mm from the impact face. Parts of plies 19 (0°) and 20 (45°) are visible, as is part of their interface. The simulation shows the corresponding plies and their interface.

determined to be in the range of 5−10 J, matrix cracks propagated along with delaminations. Fibre breakage also played a role in the damage process above an even higher energy level. These three damage modes are depicted in Figure 10.13, which shows a section of the composite specimen impacted with 19.7 J obtained by means X-ray tomography. The section of the impacted specimen was obtained at 3.6 mm from the impact face. Due to the specimen indentation, parts of plies 19 (0°) and 20 (45°) are visible in this section as well as a part of their interface. The simulation results corresponding to these two plies are also shown in this figure, and they are in good correlation with the experimental results.

Both Figures 10.9 and 10.10 show that matrix cracks parallel to the fibre directions were accurately predicted by the model, in agreement with experimental data. This was achieved because the mesh in each ply was aligned in the fibre direction. The interaction between matrix cracks and delamination is also visible in these figures: delaminations in many plies were driven or bounded by matrix cracks. In some plies, matrix cracks induced the 'jump' of the delaminations from one interface to another (e.g. 9/10 to 10/11, and 14/15 to 15/16).

## 10.4 Use case 2: high-velocity impact

Finite element models were also generated in Abaqus/Explicit to simulate the high-velocity impact of a steel sphere on an angle-ply composite laminate. The impact was normal to the laminate plane. The stacking sequence of the laminate in this case was $[0, \pm 45, 0, 90]_{4s}$ and was manufactured using T800S/M21 prepreg sheets. The total laminate thickness was 5.2 mm, and the cured ply thickness was 130 μm. VUMAT user subroutines were used to implement CDM models to simulate intraply damage, while cohesive elements with conformal meshes were used to address interply

delamination. An additional damage-activation function for out-of-plane loads based on out-of-plane shearing was introduced in the VUMAT user subroutine.

### 10.4.1 Experimental results and model definition

Coupons of 100 × 100 mm$^2$ were impacted with steel spheres of 5.5 mm diameter using a SABRE gas gun. The impact-velocity range was set to 350−550 m/s to adequately capture the ballistic limit (≈400 m/s). A Phantom V12 high-speed video camera was used to obtain the initial and residual velocities of the projectile and to determine the energy-absorption capacity of the laminate. The results of the impacts are summarized in Figure 10.14, where the residual velocity is shown against the initial impact velocity. In the simulations, the steel sphere is assumed to behave as a rigid solid, as no evidence of plastic deformation was observed after the impact tests. An initial velocity in the through-the-thickness direction of the composite plate is applied to the steel sphere within the experimental range. In addition, the edges of the laminate were simply supported, although the influence of the boundary conditions was negligible due to the high velocity of the impacts in relation to the time-of-flight of the elastic waves in reaching the boundaries.

The failure mechanisms of the impacted specimens were also studied by X-ray tomography. Figure 10.15 shows the tomogram reconstructions of one of the specimens impacted at 522 m/s, where the two main damage mechanisms, intraply and interply, are clearly identified. The high stresses arising at the impact point produced significant out-of-plane crushing and shear deformations, while evidence of fibre splitting at

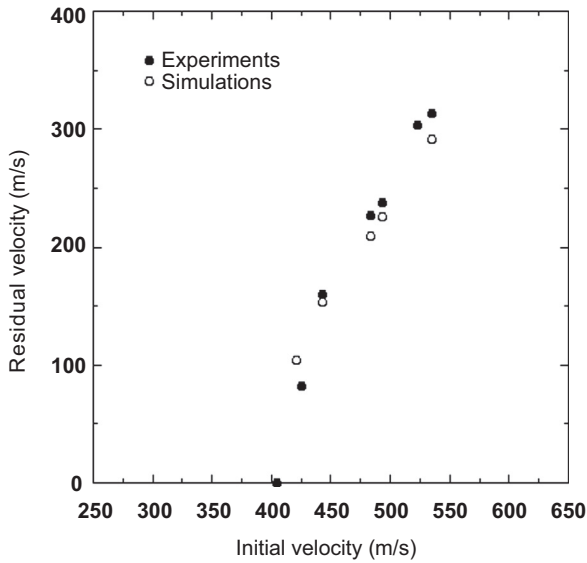


**Figure 10.14** Ballistic curve and numerical predictions for a 5.5-mm-diameter steel sphere impacting T800S/M21 composite laminate.

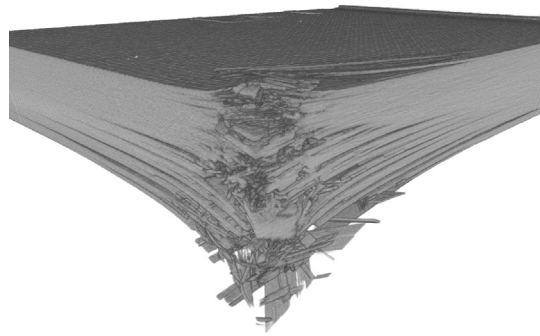

**Figure 10.15** X-ray tomography reconstruction of the specimen impacted at 522 m/s.

the rear surface due to local bending was also observed. Interply delaminations (Figure 10.17(a) were also generated by local shearing stresses at the impacted area. They were longer in the lower part of the specimen due to local bending of the remaining undamaged section, as seen in Figure 10.15. Very interestingly, the shape of the projected delaminated area was elliptical due to the laminate stacking sequence, which favoured the extension of the cracks in the 0° direction. This effect was found in all specimens that were impacted with different velocities.

The specimen was discretized with a conformal structured mesh made up of eight-node C3D8R hexahedral elements, with reduced integration using the enhanced-strain method to minimize the effect of hourglassing. The mesh was aligned with the edges of the laminate irrespective of ply orientation. COH3D8 cohesive elements were inserted at the interface between adjacent plies using a conformal mesh. Damage was localized around the impact zone, and the influence of mesh orientation on the propagation of damage was of less importance than in the low-velocity impact case. The thickness of the cohesive layer (representative of the matrix-rich region between adjacent plies) was set to 8.75 μm, a small fraction of the total ply thickness (130 μm). This was a compromise between the accuracy of the stress prediction and the excessive penalty introduced in the stable time increment during the explicit integration. Mesh regularization was carried out using a common element characteristic length, independent of the failure mechanisms, of $l_{ch}(1+, 1-, 2+, 2-, 6) = 1.0$ mm around the impact area. The element size increased towards the boundaries of the plate where the material behaviour was elastic.

Contact between the steel sphere and laminate specimen was modelled with the general contact algorithm in Abaqus/Explicit as in the previous case. Cohesive elements were removed after the corresponding damage variable reached $D = 0.99$. A Coulomb interaction between plies was introduced afterwards with a friction coefficient of $\mu = 0.3$ to model ply sliding after delamination. This element-removal mechanism also allowed for simulation of steel sphere penetration into the laminate. The use of cohesive elements with finite thickness between adjacent plies (in opposition to cohesive surfaces) introduced additional dynamic wave effects when they came into contact after cohesive elements were removed. These effects were proven to be negligible for the general penetration dynamics problem, given the small thickness of the

cohesive elements used. A total of ≈2,000,000 elements were used for the complete discretization of the specimens. Each simulation spent ≈2 days in a cluster of 40 Intel Ivy Bridge 2.6 GHz CPUs.

### 10.4.2 Simulation results

One-fourth of the deformed laminate perpendicular to the composite coupon is plotted in Figure 10.16 at 15 and 75 μs after impact, in combination with the fibre and matrix damage variables $d_1$ and $d_2$, respectively, for the case with initial velocity of 421 m/s. The impact velocity was above the ballistic limit, and therefore the laminate was fully perforated. The simulations showed that the two main damage mechanisms appeared shortly after the impact, namely out-of-plane shearing and crushing dictated by the high stresses arising at contact with the impactor sphere, and fibre tensile splitting located at the lower part of the specimen due to localized plate bending, as shown in Figure 10.16(b). Both damage mechanisms, matrix cracking and fibre breakage, were concentrated at the impact area, and only delamination extended out of bounds of the projected area of the steel sphere. The aforementioned bending effects were favoured by ply delamination that increased the local compliance of the plate around this area once the plies were fully debonded. The extension of the interply delaminations (as indicated by the interply damage parameter $D$) is shown in Figure 10.17(c), in which the contours of all delamination surfaces were superposed and compared with the X-ray tomography inspections of Figure 10.17(a). The average delamination area projection was adequately captured by the model not only in extension but also in the elliptical shape, which was slightly elongated in the 0°direction favoured by the $[0, \pm 45, 0, 90]_{4s}$ stacking sequence.

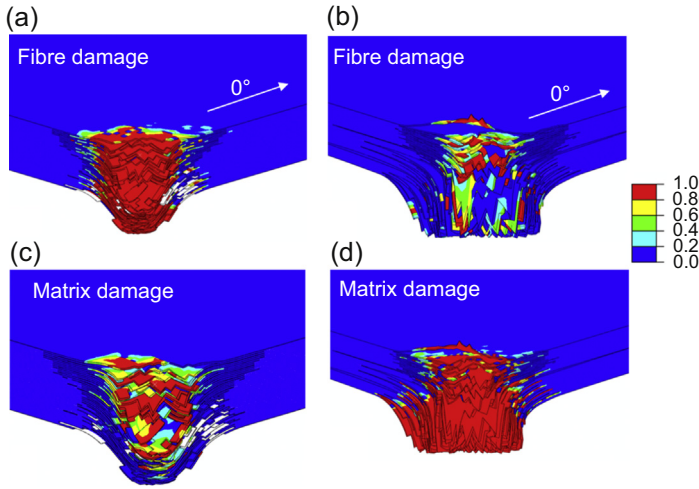


**Figure 10.16** Simulated impact at 421 m/s. Fibre damage $d_1$ at (a) $t = 15$ μs and (b) $t = 75$ μs. Matrix damage $d_2$ at (c) $t = 15$ μs and (d) $t = 75$ μs.

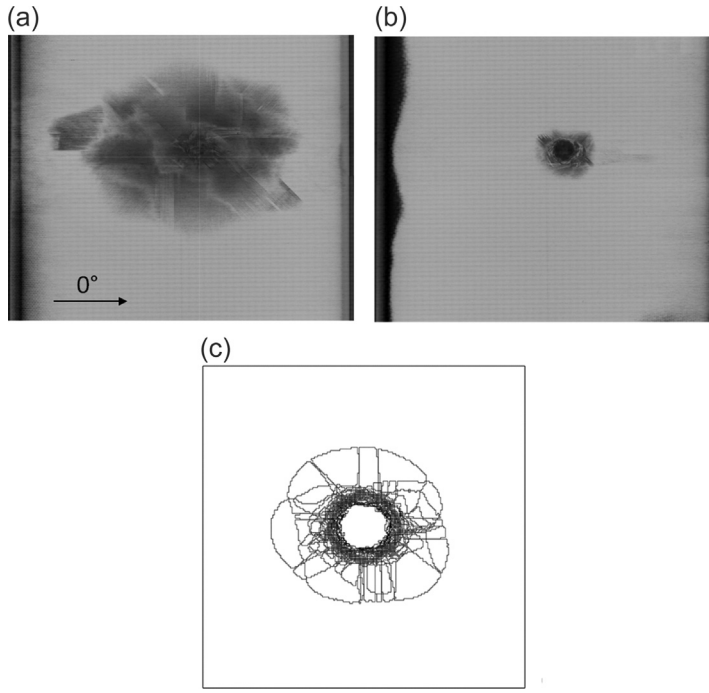


**Figure 10.17** X-ray tomography—projected delaminated areas: (a) lower half of the laminate and (b) upper half of the laminate. Simulation-projected delaminated area (c). Impact velocity 522 m/s.

The model was also able to predict the increasing number of ply delaminations in the lower half of the laminate shown in Figure 10.17(a) and (b), and Figure 10.15. Local bending effects favour these phenomena once the contact loads transmitted by the impactor are redistributed over a wider volume in the material (cone-like shape). At the beginning of the impact, delaminations were controlled by shear stresses, and propagation occurred essentially under mode II. However, once the delaminations exceeded the area directly affected by the contact stresses, propagation was mainly mode I driven and controlled by the membrane stresses in the fully debonded plies of the lower part of the laminate. The ballistic curve was computed with the model and compared with the experimental results, and was able to capture the ballistic limit of the material as well as the residual energy after in the high-velocity regime (Figure 10.14).

## 10.5 Conclusions and future trends

Computational mesomechanics is an attractive and powerful tool for determining the mechanical behaviour of angle-ply composite laminates by means of models that contain information about physical deformation and damage mechanisms. This physical enrichment allowed for establishment of the relationships among the laminate

structural unit, laminate ply, and final composite laminate. Nevertheless, computational mesomechanics requires continuous improvement in order to enhance the accuracy level, computing time and robustness of the method. The development of multiscale-based computational mechanics, where material input properties (elastic, strength and toughness) are obtained by means of the simulation and homogenization is carried out at a lower level (for instance, by means of computational micromechanics, LLorca et al., 2011) is envisaged for the near future in order to attain the specific goal of the reduction of experimental testing campaigns by means of virtual simulations. However, there are still specific areas for significant improvement in CDM, especially those related to mesh-dependency problems (mesh size, bias and direction) that limit the application field of this discipline. In the same direction as the development of multiscale models, X-FEM models have emerged that represent mesh-independent embedded cracks with minimal mesh modifications, allowing for capture of the effect of the microstructure on the intraply transverse-to-fibre failure of a unidirectional fibre−reinforced composite material. By using combined CDM models for fibre-dominated failure modes with X-FEM for matrix cracking damage, interactions among failure mechanisms can be modelled so that these models provide results consistent with experimental findings (Iarve, 2003; van der Meer & Sluys, 2009).

## Acknowledgements

This investigation was supported by the Ministerio de Economía y Competitividad of Spain through the grant MAT2012-37552, Spanish Ministry of Education grant FPU12/02087 and Airbus Spain and Centro para el Desarrollo Tecnologico Industrial CDTI through TARGET CENIT Programme 2010. In addition, the authors want to acknowledge the support of Dr Francisco Gálvez and Dr Federico Sket for some of the experimental results shown in this investigation.

## References

Abaqus, Inc. (2014). *Abaqus version 6.13 user's manual*. RI, USA: Pawtucket.

Abrate, S. (1998). *Impact on composite structures*. Cambridge, England: Cambridge University Press.

Bažant, Z. P., & Oh, B. H. (1983). Crack band theory for fracture of concrete. *Materials and Structures, 16*, 155−157. RILEM Paris.

Benzeggagh, M. L., & Kenane, M. (1996). Measurement of mixed-mode delamination fracture toughness of unidirectional glass/epoxy composites with mixed-mode bending apparatus. *Composite Science and Technology, 56*, 439.

Camanho, P. P., & Dávila, C. G. (2002). Mixed-mode decohesion finite elements for the simulation of delamination in composite materials. *NASA/TM, 2002*(211737), 1−37.

Canal, L. P., González, C., Segurado, J., & LLorca, J. (2012). Intraply fracture of fibre-reinforced composites: microscopic mechanisms and modeling. *Composite Science and Technology, 72*, 1223−1232.

Cox, B., & Yang, Q. (2006). In quest of virtual tests for structural composites. *Science, 314*, 1102.

Crews, J. H., & Reeder, J. R. (1998). *A mixed-mode bending apparatus for delamination testing*. Tech. rep. Hampton, VA: NASA, Langley Research Center. NASA/TM-100662

Dávila, C. G., Camanho, P. P., & Rose, C. A. (2005). Failure criteria for FRP laminates. *Journal of Composite Materials, 39*, 323.

González, C., & LLorca, J. (2007). Mechanical behavior of unidirectional fiber-reinforced polymers under transverse compression: microscopic mechanisms and modelling. *Composite Science and Technology, 67*, 2795−2806.

Iarve, E. V. (2003). Mesh independent modelling of cracks by using higher order shape functions. *International Journal for Numerical Methods in Engineering, 56*, 869−882.

Kachanov, L. (1986). *Introduction to continuum damage mechanics*. Springer.

Kaddour, A. S., Hinton, M. J., & Soden, P. D. (2004). A comparison of the predictive capabilities of current failure theories for composite laminates: additional contributions. *Composite Science and Technology, 64*, 449.

Lemaitre, J. (1996). *A course on damage mechanics*. Springer.

LLorca, J., González, C., Molina Aldareguía, J. M., & Lopes, C. S. (2013). Multiscale modeling of composites: toward virtual testing … and beyond. *JOM, 65*, 215−225.

LLorca, J., González, C., Molina-Aldareguía, J. M., Segurado, J., Seltzer, R., Sket, F., et al. (2011). Multiscale modeling of composite materials: a roadmap towards virtual testing. *Advanced Materials, 23*, 5130−5147.

Lopes, C. S., Seresta, O., Gürdal, Z., Camanho, P. P., & Thuis, B. (2009). Impact behaviour of dispersed stacking sequence laminates. Part I: experiments. *Composites Science and Technology, 69*, 926−936.

Maimí, P., Camanho, P. P., Mayugo, J. A., & Dávila, C. G. (2007a). A continuum damage model for composite laminates - Part I: constitutive model. *Mechanics of Materials, 39*, 897−908.

Maimí, P., Camanho, P. P., Mayugo, J. A., & Dávila, C. G. (2007b). A continuum damage model for composite laminates - Part II: computational implementation and validation. *Mechanics of Materials, 39*, 909−919.

Martin, R., Elms, T., & Bowron, S. (1998). Characterization of mode II delamination using the 4ENF. In *Proceedings of the 4th european conference on composites: Testing and standardization, Lisbon, Portugal*.

Matzenmiller, A., Lubliner, J., & Taylor, R. L. (1995). A constitutive model for anisotropic damage in fibre-composites. *Mechanics of Materials, 20*, 125.

MIL-HDBK-17-1F. (2002). Department of defense handbook, composite materials handbook. In *Polymer matrix composites, guidelines for characterization of structural materials* (Vol. 1).

Pinho, S. T., Dávila, C. G., Camanho, P. P., Iannucci, L., & Robinson, P. (2005). *Failure models and criteria for FRP under in-plane or three-dimensional stress states including shear non-linearity*. Tech. rep. Hampton, VA: NASA, Langley Research Center. NASA/TM-2005−213530.

Pinho, S. T., Iannucci, L., & Robinson, P. (2006). Physically-based failure models and criteria for laminated fibre-reinforced composites with emphasis on fibre kinking: Part I: development. *Composites Part A - Applied Science and Manufacturing, 37*, 63−73.

Pinho, S. T., Robinson, P., & Iannucci, L. (2006). Fracture toughness of the tensile and compressive fibre failure modes in laminated composites. *Composites Science and Technology, 66*, 2069−2079.

Puck, A., & Schurmann, H. (2002). Failure analysis of FRP laminates by means of physically based phenomenological models. *Composites Science and Technology, 62*, 1633−1662.

Schön, J. (2000). Coefficient of friction of composite delamination surfaces. *Wear, 237*, 77−89.

Sung, N., & Suh, N. (1979). Effect of fiber orientation on friction and wear of fiber reinforced polymeric composites. *Wear, 53*, 129−141.

Turón, A., Camanho, P. P., Costa, J., & Dávila, C. G. (2006). A damage model for the simulation of delamination in advanced composites under variable-mode loading. *Mechanics of Materials, 38*, 1072−1089.

van der Meer, F. P., & Sluys, L. J. (2009). A phantom node formulation with mixed mode cohesive law for splitting in laminates. *International Journal of Fracture, 158*, 107−124.